Bayesian *k*-Space Estimation Decreases Image Noise and Increased Activation Detection

Daniel B. Rowe, Department of Mathematical and Statistical Sciences, Marquette University

Abstract

In fMRI, as voxel sizes decrease, there is less material in them to produce a signal, leading to a decrease in the signal-to-noise ratio and contrast-to-noise ratio in each voxel. There have been many attempts to decrease the noise in an image in order to increase activation, but most lead to blurrier images. An alternative is to develop methods in spatial frequency space. Reducing noise in spatial frequency space has unique benefits. In this work, a Bayesian approach that quantifies available *a priori* information about spatial frequency coefficients, incorporates that information with observed spatial frequency coefficients, and estimates these spatial frequency coefficients *a posteriori*. Inverse Fourier transform reconstructed images from posterior estimated spatial frequency coefficients should have reduced noise and increased detection power.

1. Introduction

In magnetic resonance imaging (MRI) and functional magnetic resonance imaging (fMRI), increased spatial-temporal resolution is desired to examine detailed structures or for localization of brain activation. Increased spatial-temporal resolution is often at the cost of increased image noise. In fMRI, image processing methods such as smoothing not only decreases spatial resolution, but induces correlation between voxels (Nencka et al., 2009; Karaman et al., 2014; Rowe, 2016). Recently, approaches operating in spatial frequency *k*-space have been gaining popularity (Kornak et al., 2010a; Kornak and Young, 2010; Kornak et al. 2010b).

When Bayesian estimation is conducted in image space, pixels or voxels may be spatially correlated, and hence a spatial model is appropriate (Penny, 2005; Yu et al., 2023; Wang et al., 2024). However, it is well-known that the discrete Fourier transform of correlated pixels or voxels results in uncorrelated spatial frequency coefficients. In spatial frequency *k*-space, with each spatial frequency location being uncorrelated, they can be treated independently of each other. In MRI and fMRI, it is the spatial frequency coefficients that are measured independently with analog-to-digital converters (ADCs), so they are inherently statistically independent. One consequence of the fMRI spatial frequency coefficients being measured is that the array does not possess Hermitian symmetry, leading to complex-valued images (Rowe and Logan 2004; Rowe 2005).

In fMRI, Bayesian estimation of spatial frequency coefficients has been performed in Cartesian coordinates with the use of a bivariate normal distribution with phase coupled means (Sakitis et al., 2024). An interesting alternative, the Bayesian image analysis in Fourier space (BIFS) performs Bayesian estimation of spatial frequency coefficients in polar coordinates (Kornak et al., 2024). The methods herein are similar, but utilize conjugate prior distributions, which leads to simpler estimation.

2. Methods

2.1 Likelihood

Spatial frequency coefficient measurements in an array of *k*-space are complex-valued consisting of real and imaginary parts. It is well-known that the real k_R and imaginary k_I parts of a given spatial frequency coefficient contains additive independent and identically distributed normal noise, $k_R \sim N(\rho\cos\theta,\sigma^2)$ and $k_I \sim N(\rho\sin\theta,\sigma^2)$. The bivariate distribution of the real and imaginary parts can be expressed as in Equation 1

$$f(k_R,k_I \mid \rho,\theta,\sigma^2) = \frac{1}{(2\pi\sigma^2)^{1/2}}\exp\left[-\frac{(k_R-\rho\cos\theta)^2}{2\sigma^2}\right]\frac{1}{(2\pi\sigma^2)^{1/2}}\exp\left[-\frac{(k_I-\rho\sin\theta)^2}{2\sigma^2}\right] \quad (1)$$

where the means are coupled by the phase. We can express the complex-valued spatial frequency coefficients in terms of polar coordinates of magnitude and phase. A transformation from Cartesian random variables (k_R,k_I) to polar random variables (r,ϕ), where $k_R=r\cos(\phi)$, $k_I=r\sin(\phi)$ and Jacobian is $J=r$ is performed to arrive at a joint distribution

$$f(r,\phi \mid \rho,\theta,\sigma^2) = \frac{r}{2\pi\sigma^2}\exp\left\{-\frac{1}{2\sigma^2}\left[r^2+\rho^2-2r\rho\cos(\phi-\theta)\right]\right\}. \tag{2}$$

From this bivariate distribution of magnitude and phase in Equation 2, the Ricean marginal distribution for the magnitude with location ρ and scale σ in Equation 3

$$f(r \mid \rho,\sigma^2) = \frac{r}{\sigma^2}\exp\left\{-\frac{r^2+\rho^2}{2\sigma^2}\right\} I_0\left(\frac{r\rho}{\sigma^2}\right) \tag{3}$$

can be derived, where $I_0(\cdot)$ is the modified Bessel function of the first kind with order zero (Rice, 1944; Gudbjartsson and Patz, 1995). Further, the unnamed non-normal marginal distribution in Equation 4

$$f(\phi \mid \rho,\theta,\sigma^2) = \frac{1}{2\pi}\exp\left[-\frac{\rho^2}{2\sigma^2}\right]\left[1+\frac{\rho}{\sigma}\sqrt{2\pi}\cos(\phi-\theta)\exp\left[\frac{\rho^2\cos^2(\phi-\theta)}{2\sigma^2}\right]\Phi\left(\frac{\rho\cos(\phi-\theta)}{\sigma}\right)\right] \tag{4}$$

for the phase can be found, where $\Phi(\cdot)$ is the cumulative distribution function of the standard normal distribution (Gudbjartsson and Patz, 1995; Rowe and Logan, 2004). The mean and variance of the Rice distribution do not have simple forms and involve a Laguerre polynomial. When the true magnitude ρ is zero (i.e. no contribution from the spatial frequency) usually at large spatial frequencies, the Ricean distribution becomes the Rayleigh distribution with mean $\sigma\sqrt{(\pi/2)}$ and variance $\sigma^2(4-\pi)/2$. When true magnitude ρ is large (i.e. a large contribution from the spatial frequency) usually nearer to the zero frequency, it becomes the normal distribution with mean ρ and variance σ^2. Generally $\rho/\sigma>3$, is considered sufficient for the normal limiting distribution. When the true phase θ is zero (no contribution from the spatial frequency), the unnamed non-normal distribution becomes the uniform distribution between $-\pi$ and π and with mean 0 and variance $\pi^2/3$. When true magnitude ρ is very large (a large contribution from the spatial frequency) the phase distribution in Equation 4 becomes the normal distribution with mean θ and variance $(\sigma/\rho)^2$.

We can express the bivariate magnitude and phase distribution as the product of the marginal distribution for the magnitude and the conditional distribution of the phase given the magnitude as

$$f(r,\phi \mid \rho,\theta,\sigma^2) = f(r \mid \rho,\sigma^2)\, f(\phi \mid r,\rho,\theta,\sigma^2). \tag{5}$$

It can be shown that the conditional distribution of the phase ϕ given the magnitude r is von Mises (von Mises, 1918; Wikipedia 2024a) with location θ and scale $r\rho/\sigma^2$,

$$f(\phi \mid r,\rho,\theta,\sigma^2) = \frac{\exp\left\{\frac{r\rho\cos(\phi-\theta)}{\sigma^2}\right\}}{2\pi I_0\left(\frac{r\rho}{\sigma^2}\right)}. \tag{6}$$

Using the marginal distribution of the magnitude and conditional distribution of the phase given the magnitude, the joint distribution of the magnitude and phase is

$$f(r,\phi \mid \rho,\theta,\sigma^2) = \frac{r}{\sigma^2}\exp\left\{-\frac{r^2+\rho^2}{2\sigma^2}\right\} I_0\left(\frac{r\rho}{\sigma^2}\right)\cdot\frac{\exp\left\{\frac{r\rho\cos(\phi-\theta)}{\sigma^2}\right\}}{2\pi I_0\left(\frac{r\rho}{\sigma^2}\right)}. \tag{7}$$

In summary, the distributions for the data are $r \sim R(\rho,\sigma)$ and $\phi|r \sim VM(\theta, r\rho/\sigma^2)$.

2.2 Priors

Utilizing the same family of distributions for the prior distributions, the prior distribution for the magnitude $\rho|\sigma^2$ is Ricean with location ρ_0 and scale $\sigma/\sqrt{\gamma}$,

$$f(\rho \mid \rho_0, \sigma^2, \gamma) = \frac{\rho}{\sigma^2/\gamma} \exp\left\{-\frac{\rho^2+\rho_0^2}{2\sigma^2/\gamma}\right\} I_0\left(\frac{\rho\rho_0}{\sigma^2/\gamma}\right). \tag{8}$$

The Ricean prior distribution becomes the Rayleigh distribution when $\rho_0=0$ and the normal distribution when $\rho_0 >> 0$, generally $\rho_0/\sigma > 3$ is considered sufficient. This Ricean prior distribution becomes vague with a very small γ. Additionally, using the same family, the prior distribution for the phase θ given the magnitude ρ and residual variance σ^2 is is von Mises with location θ_0 and scale $\rho\rho_0/(\sigma^2/\gamma)$,

$$f(\theta \mid \rho, \sigma^2, \theta_0, \gamma) = \frac{\exp\left\{\frac{\rho\rho_0 \cos(\theta-\theta_0)}{\sigma^2/\gamma}\right\}}{2\pi I_0\left(\frac{\rho\rho_0}{\sigma^2/\gamma}\right)}. \tag{9}$$

This von Mises prior distribution becomes the uniform distribution on $(-\pi, \pi)$ when $\rho_0=0$ and the normal distribution for large $\rho\rho_0/(\sigma^2/\gamma)$. The von Mises prior distribution becomes vague with a very small γ. Further, we can assess a prior distribution for the variance σ^2 with an inverse gamma distribution

$$f(\sigma^2 \mid \alpha, \beta) = \frac{\beta^\alpha}{\Gamma(\alpha)(\sigma^2)^{\alpha+1}} \exp\left\{-\frac{\beta}{\sigma^2}\right\}. \tag{10}$$

The inverse gamma prior distribution becomes a vague prior with very small α and β. In summary, the prior distributions are $\rho|\sigma^2 \sim R(\rho_0,\sigma/\sqrt{\gamma})$, $\theta|\rho,\sigma^2 \sim VM(\theta_0, \rho\rho_0/(\sigma^2/\gamma))$, and $\sigma^2 \sim IG(\alpha,\beta)$.

2.3 Posterior

Upon combining the priors in Equations 8-10 and the likelihood in Equation 7, the posterior distribution becomes

$$f(\rho,\theta,\sigma^2 \mid r,\phi) \propto f(\rho \mid \sigma^2, \rho_0, \gamma)\, f(\theta \mid \rho, \sigma^2, \theta_0, \gamma)\, f(\sigma^2 \mid \alpha, \beta)\, f(r \mid \rho, \sigma^2)\, f(\phi \mid r, \rho, \theta, \sigma^2) \tag{11}$$

$$\begin{aligned} f(\rho,\theta,\sigma^2 \mid r,\phi) \quad \propto \quad & \frac{\rho}{\sigma^2} \exp\left\{-\frac{\rho^2+\rho_0^2}{2\sigma^2/\gamma}\right\} I_0\left(\frac{\rho\rho_0}{\sigma^2/\gamma}\right) \frac{\exp\left\{\frac{\rho\rho_0\cos(\theta-\theta_0)}{\sigma^2/\gamma}\right\}}{2\pi I_0\left(\frac{\rho\rho_0}{\sigma^2/\gamma}\right)} \frac{\beta^\alpha}{\Gamma(\alpha)(\sigma^2)^{\alpha+1}} \exp\left\{-\frac{\beta}{\sigma^2}\right\} \\ & \times \frac{r}{\sigma^2} \exp\left\{-\frac{r^2+\rho^2}{2\sigma^2}\right\} I_0\left(\frac{r\rho}{\sigma^2}\right) \frac{\exp\left\{\frac{r\rho\cos(\phi-\theta)}{\sigma^2}\right\}}{2\pi I_0\left(\frac{r\rho}{\sigma^2}\right)}. \end{aligned} \tag{12}$$

Some simplification leads to the joint posterior distribution

$$f(\rho,\theta,\sigma^2 \mid r,\phi) \propto \frac{\beta^{\alpha} r}{\Gamma(\alpha)} \exp\left\{-\frac{1}{2\sigma^2}\left[\gamma\rho_0^2 + r^2 + 2\beta\right]\right\} \times \frac{\rho}{(\sigma^2)^{\alpha+3}} \exp\left\{-\frac{1}{2\sigma^2}\left[(\gamma+1)\rho^2 - 2\rho\left(\rho_0\gamma\cos(\theta-\theta_0) + r\cos(\phi-\theta)\right)\right]\right\}. \quad (13)$$

The posterior conditional distributions can be found by only considering terms that contain our parameter of interest. It can be shown that the posterior conditional distribution of ρ given θ and σ^2 is a Modified Half Normal (Sun et al., 2021; Wikipedia, 2024b)

$$f(\rho \mid \theta,\sigma^2,r,\phi) = \frac{2B^{A/2}\rho^{A-1}}{\Psi\left(\frac{A}{2},\frac{C}{\sqrt{B}}\right)} \exp\left\{-B\rho^2 + C\rho\right\} \quad (14)$$

where $\Psi(A/2,C/\sqrt{B})$ denotes the Fox-Wright Psi function (Fox, 1928; Wright, 1935), A=2, B=$(\gamma+1)/(2\sigma^2)$, and C=$[\rho_0\gamma\cos(\theta-\theta_0)+r\cos(\phi-\theta)]/\sigma^2$. Further, it can be shown that the posterior conditional distribution of θ given ρ and σ^2 is

$$f(\theta \mid \rho,\sigma^2,r,\phi) \propto \exp\left\{\frac{\rho}{\sigma^2}\left[\rho_0\gamma\cos(\theta-\theta_0) + r\cos(\phi-\theta)\right]\right\}. \quad (15)$$

Utilizing some trigonometric identities (Wikipedia, 2024c) as outlined in the Appendix, this becomes the von Mises distribution with location λ and scale κ,

$$f(\theta \mid \rho,\sigma^2,r,\phi) = \frac{\exp\{\kappa\cos(\theta-\lambda)\}}{2\pi I_0(\kappa)} \quad (16)$$

where $\kappa=c\rho/\sigma^2$, $a=\rho_0\gamma\cos(\theta_0)+r\cos(\phi)$, $b=\rho_0\gamma\sin(\theta_0)+r\sin(\phi)$, $c=\text{sign}(a)\sqrt{(a^2+b^2)}$, and $\lambda=\arctan(b/a)$. The posterior conditional distribution of σ^2 given θ and ρ is an inverse gamma distribution (Wikipedia, 2024d) with parameters $\alpha^*=\alpha+2$ and $\beta^*=\{(\gamma+1)\rho^2-2\rho[\rho_0\gamma\cos(\theta-\theta_0)+r\cos(\phi-\theta)]+(\gamma\rho_0^2+r^2+2\beta)\}/2$

$$f(\sigma^2 \mid \rho,\theta,r,\phi) = \frac{(\beta^*)^{\alpha^*}}{\Gamma(\alpha^*)(\sigma^2)^{\alpha^*+1}} \exp\left(-\frac{\beta^*}{\sigma^2}\right). \quad (17)$$

In summary, the posterior conditional distributions are $\rho|\theta,\sigma^2 \sim MHN(A,B,C)$, $\theta|\rho,\sigma^2 \sim VM(\lambda,\kappa)$, and $\sigma^2|\rho,\theta \sim IG(\alpha^*,\beta^*)$.

2.4 Estimation

At each k-space spatial frequency location, we individually estimate the magnitude and phase of the associated amplitude coefficient. Since we have the posterior conditional distributions, we can perform a Gibbs sampling to obtain the entire distribution (Geman and Geman, 1984; Gelfand and Smith, 1990) and compute the marginal posterior mean (MPM), however, when only one value is needed such as the mode, we can use the iterated conditional modes (ICM) algorithm (Lindley and Smith, 1972; O'Hagan, 1994) for maximum *a posteriori* (MAP).
The modes of the posterior conditional distributions are

$$\hat{\rho} = \frac{C + \sqrt{C^2 + 8B(A-1)}}{4B} \quad (18)$$

where A=2, B=$(\gamma+1)/(2\sigma^2)$, C=$[\rho_0\gamma\cos(\theta-\theta_0)+r\cos(\phi-\theta)]/\sigma^2$,

$$\hat{\theta} = \arctan\left(\frac{b}{a}\right) \tag{19}$$

where $a=\rho_0\gamma\cos(\theta_0)+r\cos(\phi)$, $b=\rho_0\gamma\sin(\theta_0)+r\sin(\phi)$, and

$$\hat{\sigma}^2 = \frac{\beta^*}{\alpha^*+1} \tag{20}$$

where $\alpha^*=\alpha+2$ and $\beta^*=\{(\gamma+1)\rho^2-2\rho[\rho_0\gamma\cos(\theta-\theta_0)+r\cos(\phi-\theta)]+(\gamma\rho_0^2+r^2+2\beta)\}/2$.

The ICM algorithm proceeds by starting with initial values for the parameters, then iteratively computing each giving the other similar to a Gibbs sampler, until convergence is reached. If there is a unique global maxima, the iterative parameter estimates will converge to it.

3. Experimental Results

Experimental data is from a block design right-hand finger tapping experiment on a 3.0-Tesla General Electric Signa LX MRI scanner. The imaging parameters were n_z=7 slices of 2.5 mm thick and 128×128 array size with a field-of-view FOV=24.0 cm, echo time TE=60.4 ms, effective echo spacing EESP=0.832 ms, and time-of-repetition TR= 1 s. The experiment timing followed an initial 16 s of rest followed by 19 epochs of 16 s of task alternating with 16 s of rest resulting in a total of n_t=624 total image volumes. Each slice image at each time point, was Nyquist ghost corrected (Nencka, et al., 2008). Images were phase drift corrected by calculating the angular phase temporal mean of each voxel's time-series, then subtracting it from each voxel time-series. A local second order polynomial was spatially fit to the resultant difference of the phase time-series slice images. Then the fitted polynomial is subtracted from the original phase image producing a steady phase over time for each coil (Sakitis and Rowe, 2024).

Figure 1 presents the real k_R and imaginary k_I parts of the spatial frequency k-space array for the t=1 time point of slice 2 in the third column, pre-multiplied by an IDFT matrix in the second column, post-multiplied by the transpose of an IFT matrix reconstructed matrix in the fourth column, reconstructed into a real and imaginary image in the first column.

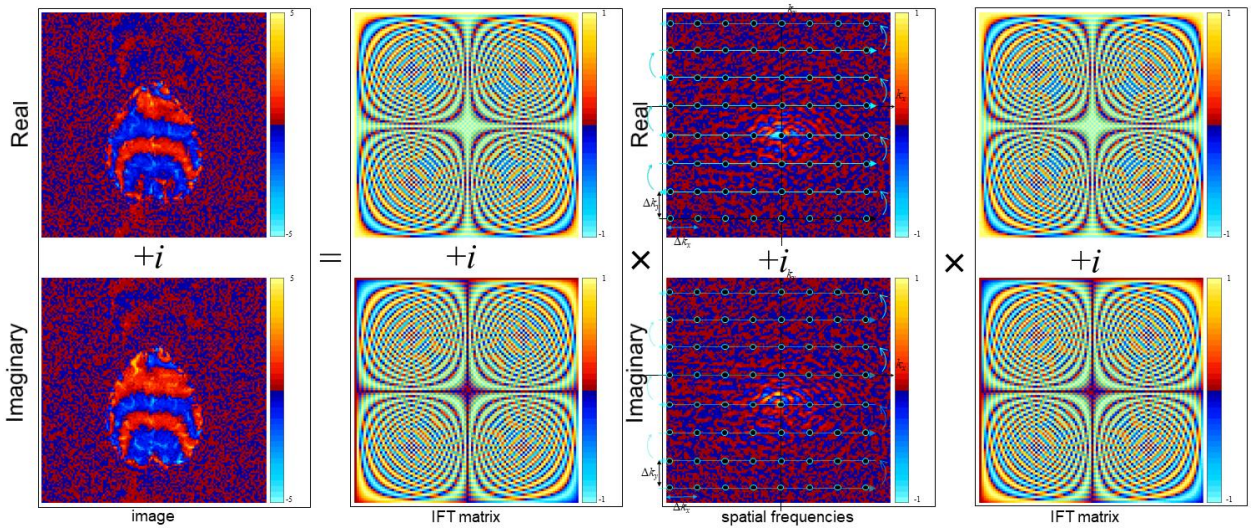

Figure 1: Slice 2 k-space array for first time point IFT reconstructed into a real-imaginary image.

Figure 2 represents the magnitude r and phase ϕ parts of the spatial frequency k-space array for the t=1 time point of slice 2 in the third column, pre-multipled by an IDFT matrix in the second column, post-multiplied by the transpose of an IFT matrix reconstructed matrix in the fourth column, reconstructed into a magnitude and phase image in the first column.

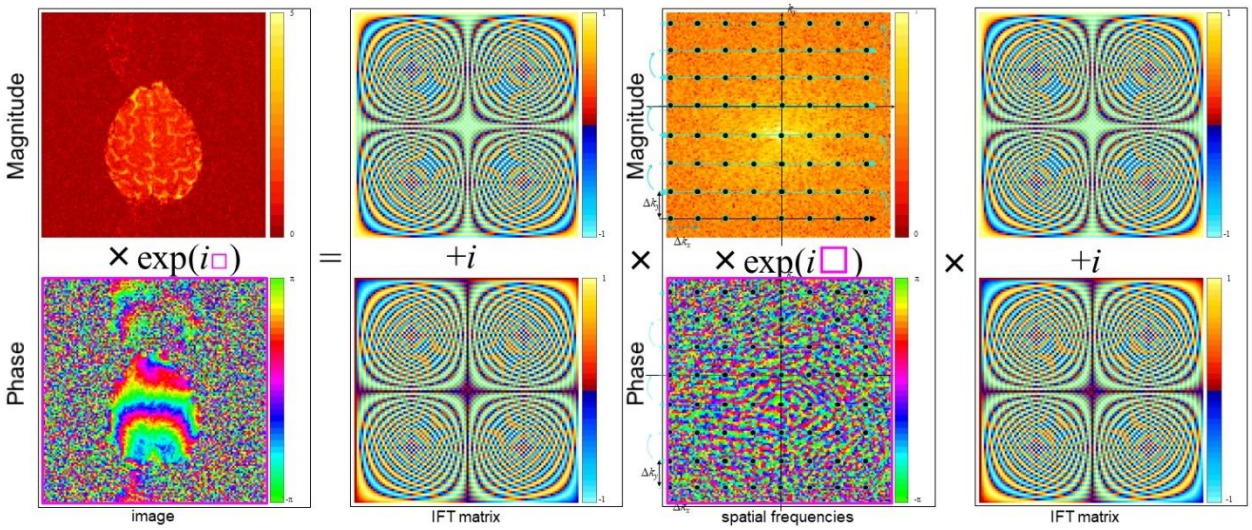

Figure 2: Slice 2 *k*-space array for first time point IFT reconstructed into a magnitude-phase image.

The first three volume images have decreasing intensity with TR and not homogeneous with the remaining images. Figure 3 illustrates this image intensity equilibration phenomenon for times *t*=1-4 of slice 2. In Figure 3, the magnitude is in the top row and the phase is in the bottom row.

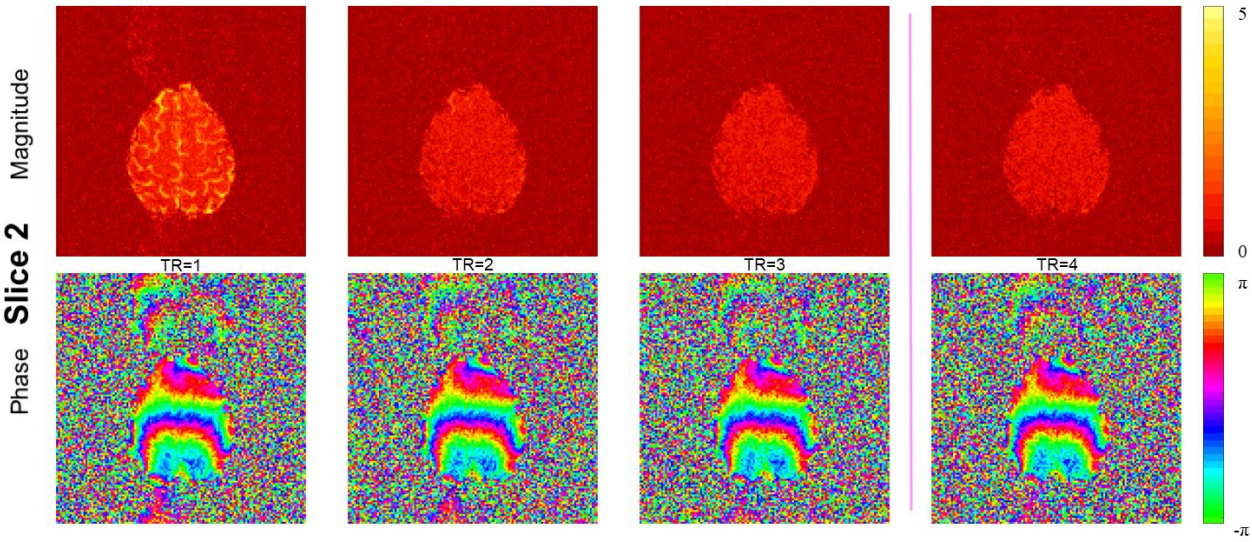

Figure 3: First four reconstructed images in columns for slice 2 with magnitude in top row and phase in bottom row.

With the first three volume images have decreasing intensity with TR, we can also see this phenomenon in the center of their *k*-space arrays. Figure 4 illustrates this center of *k*-space intensity equilibration phenomenon for times *t*=1-4 of slice 2 in real and imaginary. In Figure 4, the real is in the top row and the imaginary is in the bottom row.

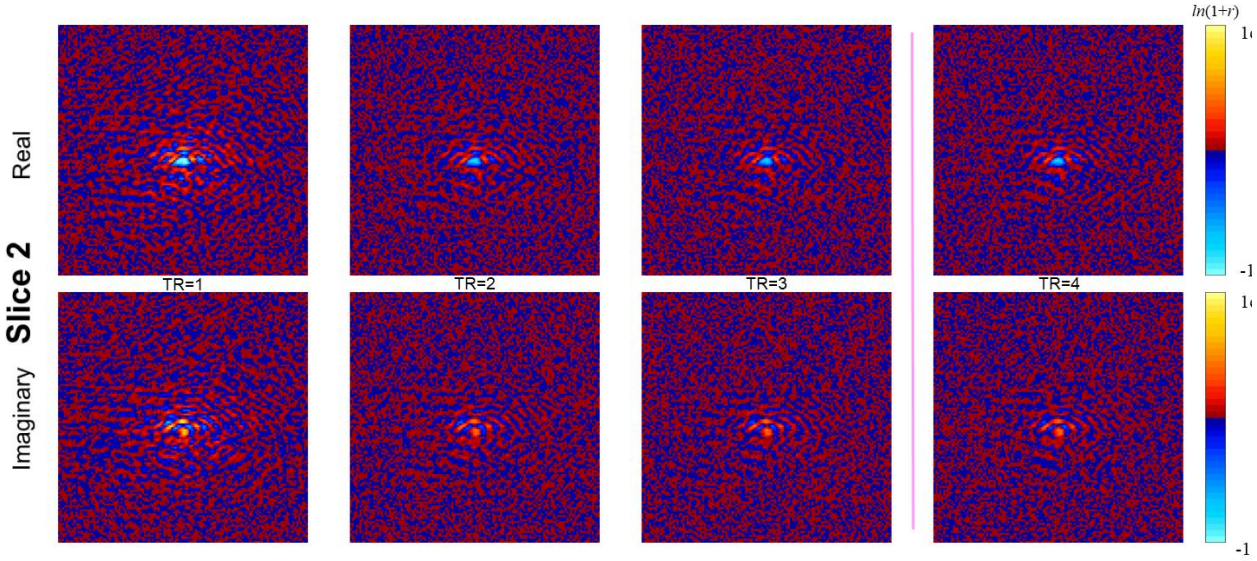

Figure 4: First four *k*-space images in columns for slice 2 with real in top row and imaginary in bottom row.

Figure 5 also illustrates this center of *k*-space intensity equilibration phenomenon for times t=1-4 of slice 2 in magnitude and phase. In Figure 5, the magnitude is in the top row and the phase is in the bottom row. Note that the intensity of the center of *k*-space decreases over time.

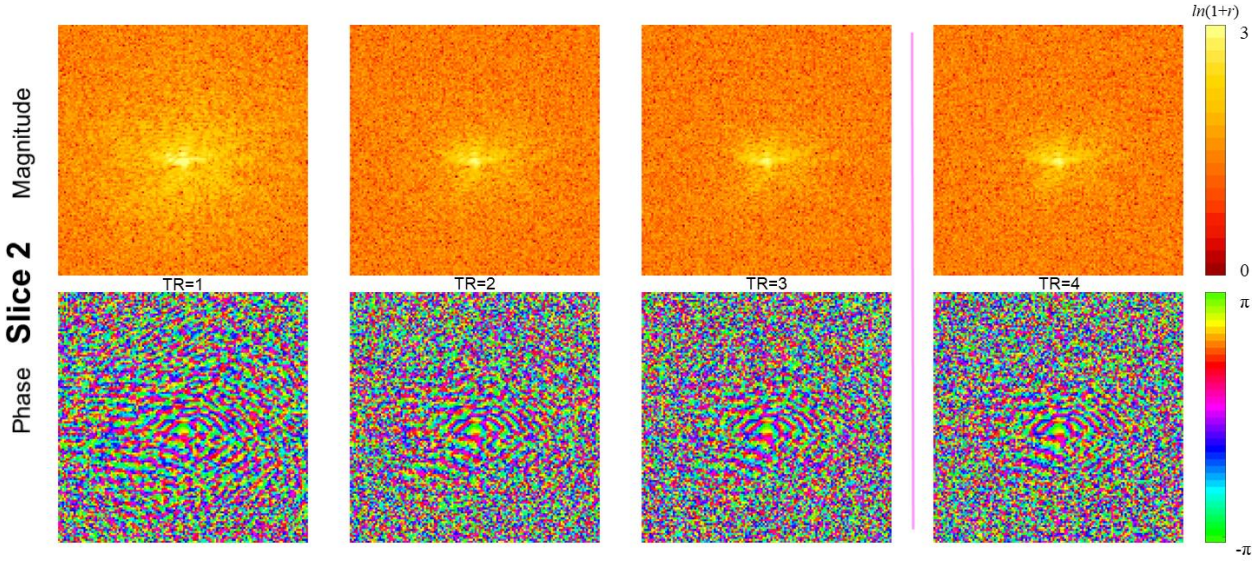

Figure 5: First four *k*-space images for slice 2 with magnitude in top row and phase in bottom row.

In fMRI, the standard practice, is to omit the first three volume images when computing activation due to machine magnetic field equilibration, which would result in n=621 images (images 4-624). The magnitude of all n_z =7 slices for time t=4 is presented in Figure 6. The images for times 5-624 are all visually similar to those at time 4.

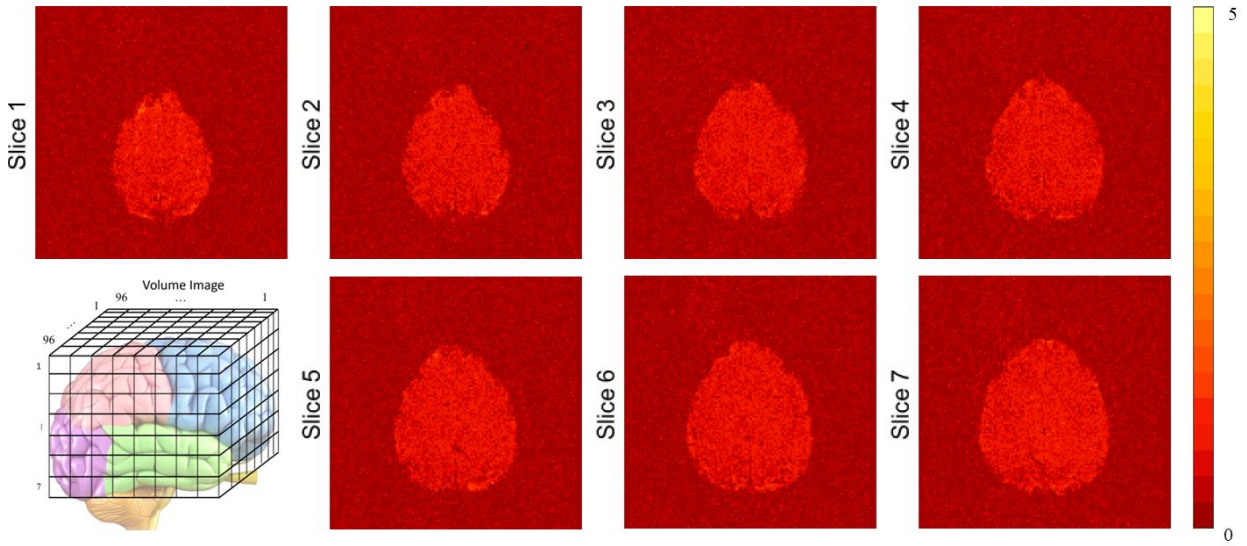

Figure 6: Magnitude of reconstructed images for n_z =7 slices at time t=4.

However, the first three "prior" images, the first three columns in Figures 4-6 are ideal to use to assess hyperparameters of prior distributions to combine with each TR volume image. At each k-space location, the first three complex-valued (magnitude and phase) k-space arrays as shown in the first three columns of Figure 4 were averaged to produce mean real and imaginary volume images, $\bar{k}_R$ and $\bar{k}_I$.

At each k-space location, the magnitude of the averaged complex-valued prior k-space arrays was computed for the prior mean $\rho_0=\sqrt{\bar{k}_R^2+\bar{k}_I^2}$ and presented in Figure 7.

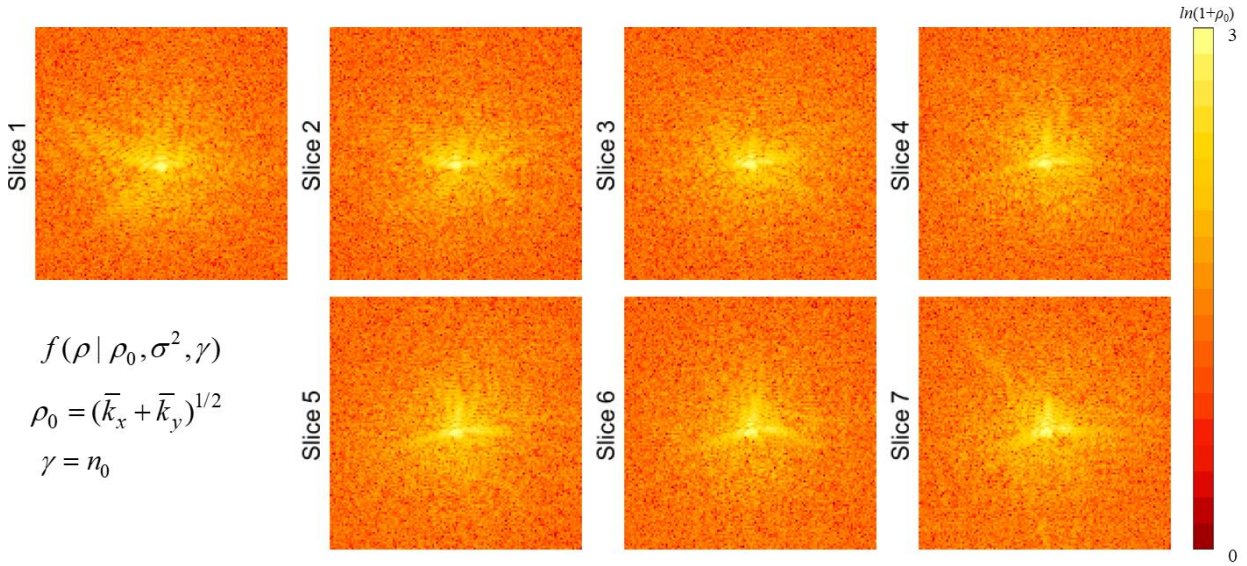

Figure 7: Prior k-space hyperparameter ρ_0 for n_z =7 slices.

At each k-space location, the four-quadrant arctangent of the averaged complex-valued prior k-space arrays was computed for the prior mean $\theta_0=\arctan_4(\bar{k}_I / \bar{k}_R)$ as presented in Figure 8 while the prior scaling coefficient $\gamma=n_0=3$.

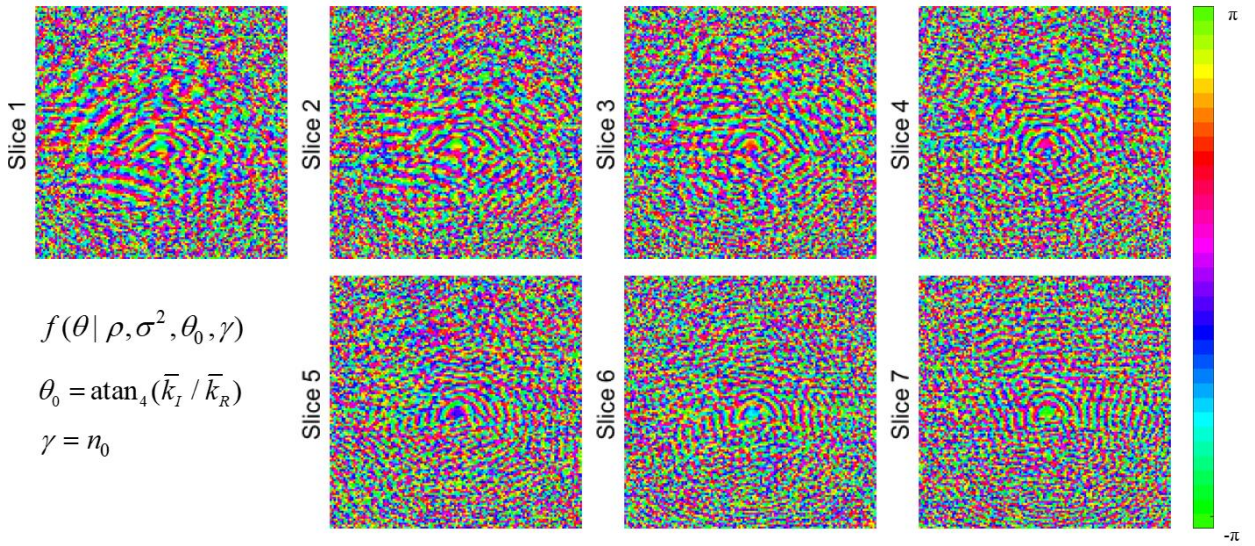

Figure 8: Prior *k*-space hyperparameter θ_0 for n_z =7 slices.

At each *k*-space location, the prior distribution quantity $\sigma_0^2 = (s_R^2 + s_I^2)/2$ is computed as the averaged variance of the real and imaginary prior *k*-space arrays as shown in Figure 9. The prior shape and scale parameters are assessed to be α=n_0-1=2 and β=(n_0-1) σ_0^2 =2 σ_0^2 , is simply a scaled version of the prior variance in Figure 9 and not displayed.

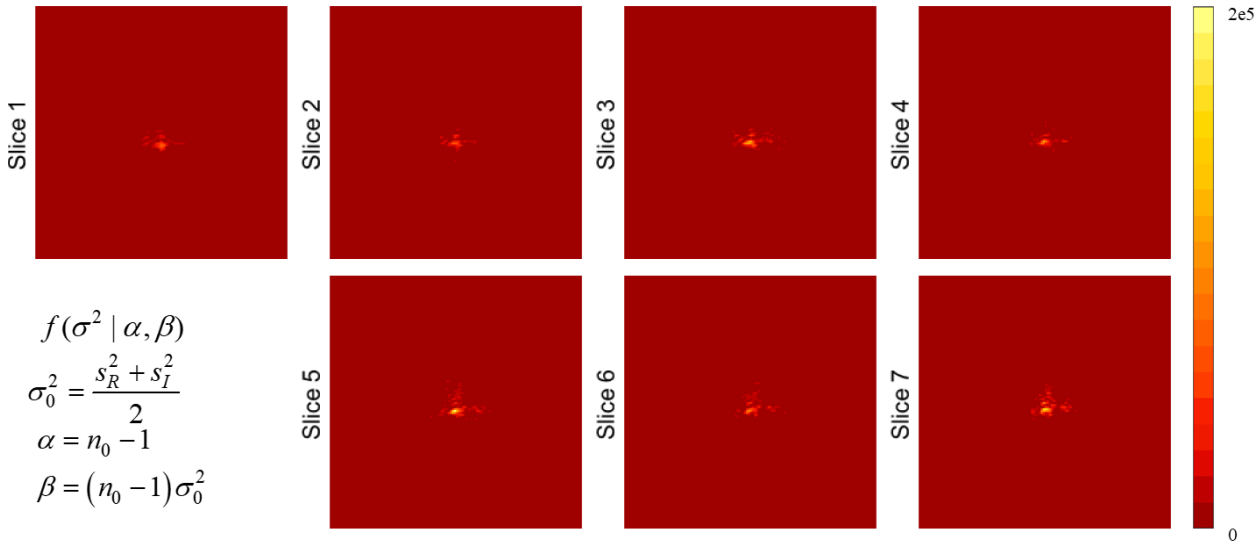

Figure 9: Prior *k*-space hyperparameter σ_0^2 for n_z =7 slices.

Maximum a posterior (MAP) estimates were calculated using the ICM algorithm. An initial value for $\hat{\sigma}^2$ was selected and a new modal value for $\hat{\theta}$ computed from Equation 19, then given the initial value for $\hat{\sigma}^2$ and the new modal value for $\hat{\theta}$, a new modal value for $\hat{\rho}$ is computed from Equation 18, then given the new modal values for $\hat{\theta}$ and $\hat{\rho}$, new modal value for $\hat{\sigma}^2$ computed from Equation 20. This process proceeds as $\hat{\sigma}^2_{(0)}$, $(\hat{\theta}_{(1)}, \hat{\rho}_{(1)}, \hat{\sigma}^2_{(1)})$,…., $(\hat{\theta}_{(L)}, \hat{\rho}_{(L)}, \hat{\sigma}^2_{(L)})$ until convergence where the parenthesed subscript indicates the iteration number. The last

convergence value is our MAP estimator. In practice it only took L=3 iterations to achieve convergence, but the algorithm was run to L=10.

The Bayesian k-space magnitude phase estimation was applied to all slices in the time 4 volume image in Figure 6. In Figure 10 the posterior estimated k-space magnitude is displayed. We can see that the posterior k-space magnitude image for slice 2 has increased intensity at the center of k-space as compared to the likelihood image in the first row and fourth column of Figure 5.

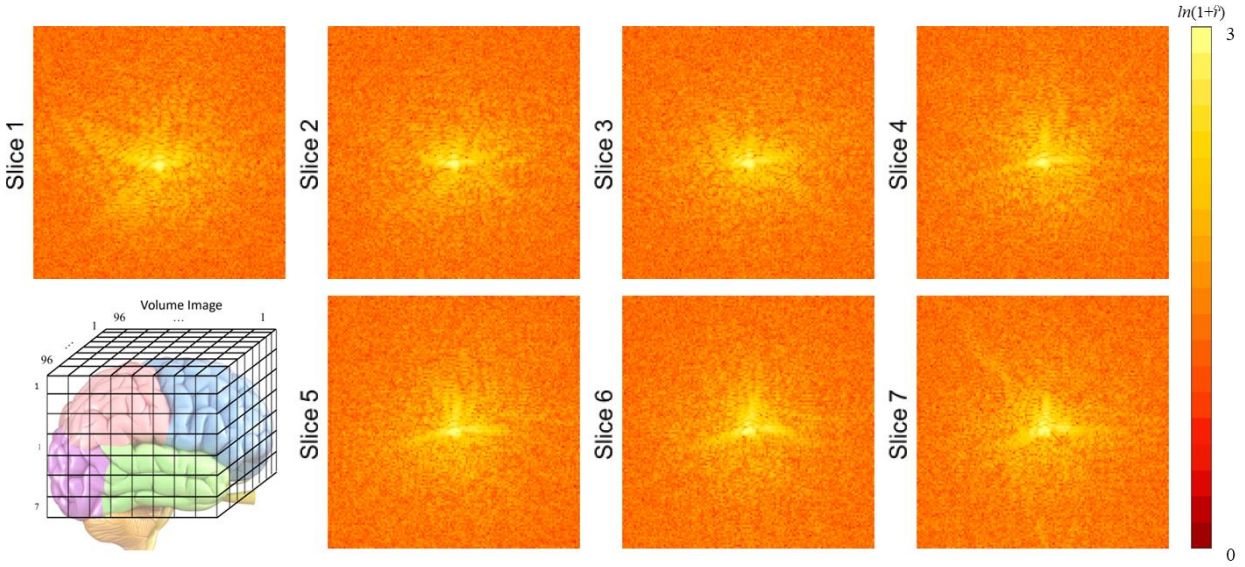

Figure 10: Posterior MAP estimated k-space magnitude for n_z =7 slices at time t=4.

In Figure 11 the posterior estimated k-space phase is displayed. We can see that the posterior k-space phase image for slice 2 looks very similar near the center of k-space as compared to the likelihood k-space image in the second row and fourth column of Figure 5 with marginally increased structure near the center.

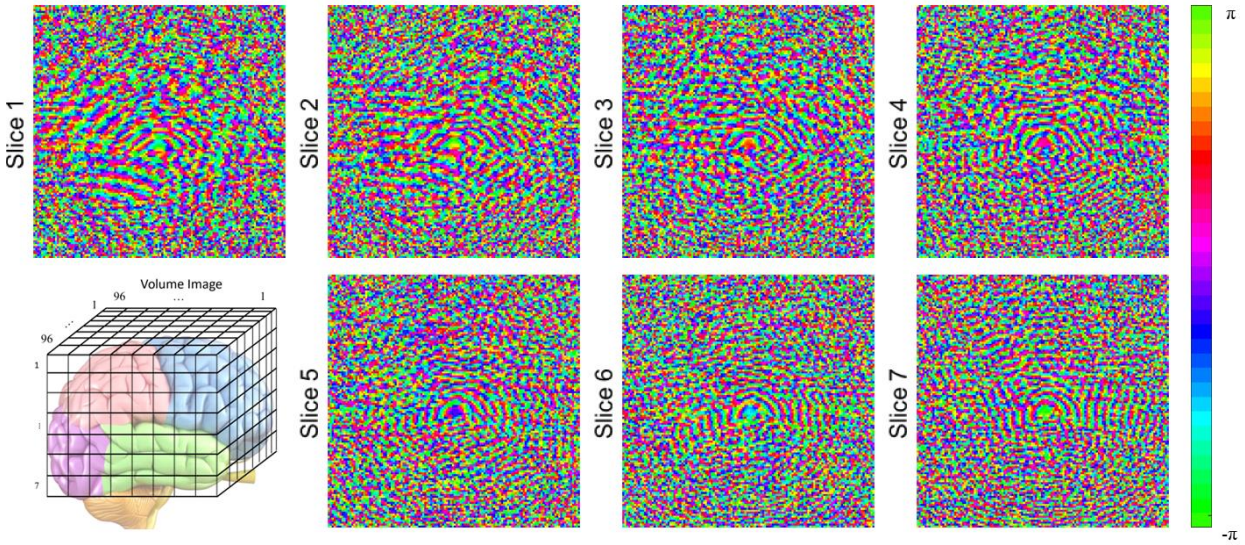

Figure 11: Posterior MAP estimated k-space phase for n_z =7 slices at time t=4.

The posterior estimate of the k-space variance was also computed and displayed in Figure 12. The variance is much lower than the likelihood variance (not shown) and the prior variances in Figure 9.

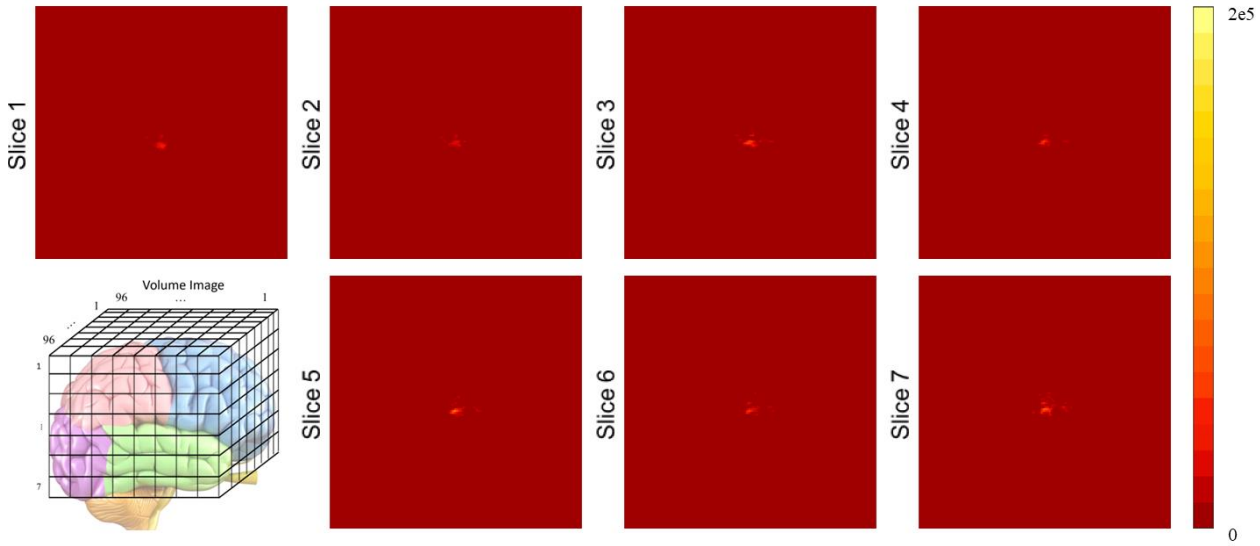

Figure 12: Posterior MAP estimated *k*-space variance for n_z =7 slices at time t=4.

The posterior estimated *k*-space magnitude arrays in Figure 10 were combined with the posterior estimated *k*-space phase arrays Figure 11 and IFT reconstructed into images. The posterior magnitude images are in Figure 13. We can compare the Bayesian posterior estimated images in Figure 14 to the likelihood image in Figure 6 and see that the posterior images are sharper, brighter, and less noisy.

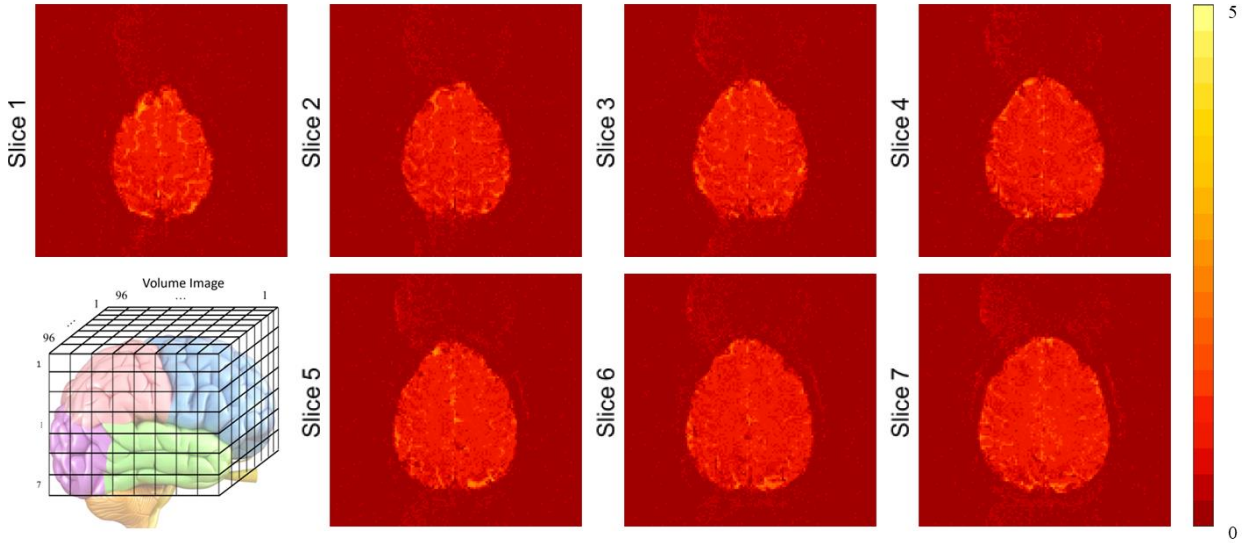

Figure 13: Posterior MAP estimated image magnitude for n_z =7 slices at time t=4.

The posterior phase images are in Figure 14. We can see that the posterior phase image for slice 2 in the first row and second column looks similar to the likelihood image in the second row and fourth column of Figure 3 but with less noise, albeit with enhanced ghosting signal artifact.

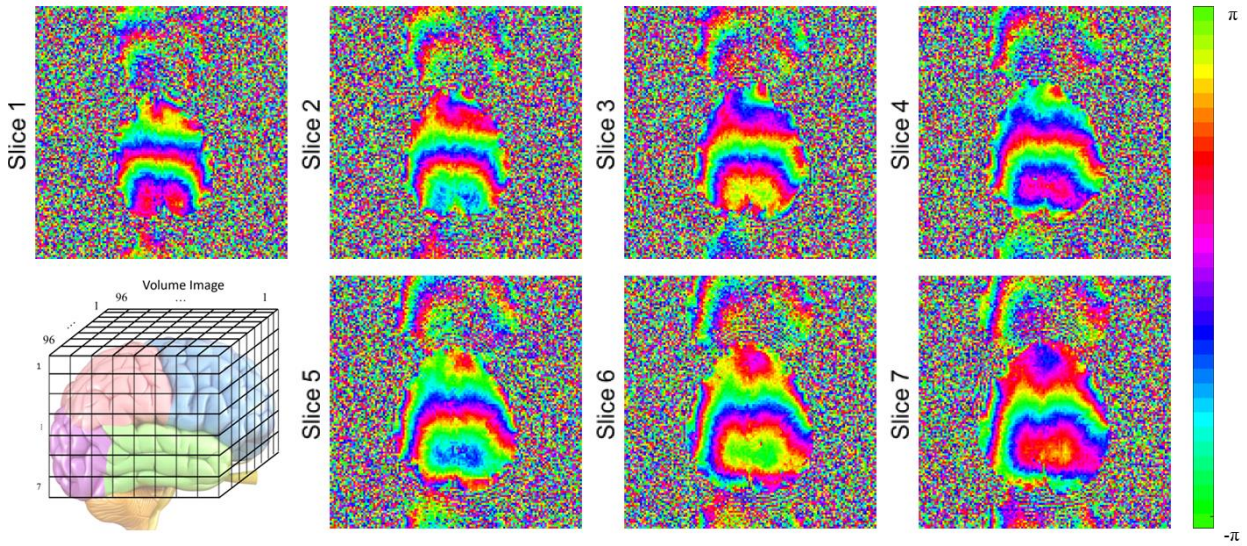

Figure 14: Posterior MAP estimated image phase for n_z =7 slices at time t=4.

4. Conclusions

A Bayesian approach was presented to utilize the first three discarded images to yield an improved *k*-space array estimate that is IFT reconstructed into an image. The Bayesian procedure used conjugate prior distributions in polar coordinates. The MAP estimation from the posterior distribution is straightforward with minimal computation necessary. Posterior images are brighter, have greater contrast, and lower noise. Future work involved applying the Bayesian *k*-space estimation to an entire volume image series and calculating activation. It is anticipated that in addition to increased intensity, contrast, and reduced noise, that there will be increased activation.

Appendix

The bracketed term in the exponent of Equation 15 can be simplified using well-known trigonometric identities (Wikipedia, 2024c). First the angle difference identities applied

$$\begin{aligned} r\cos(\phi-\theta) &= r[\cos(\phi)\cos(\theta)+\sin(\phi)\sin(\theta)] \\ \rho_0\gamma\cos(\theta-\theta_0) &= \rho_0\gamma[\cos(\theta)\cos(\theta_0)+\sin(\theta)\sin(\theta_0)] \end{aligned}$$

then the multiplicative terms distributed and sinusoidal terms containing θ collected

$$r\cos(\phi-\theta)+\rho_0\gamma\cos(\theta-\theta_0)=[r\cos(\phi)+\rho_0\gamma\cos(\theta_0)]\cos(\theta)+[r\sin(\phi)+\rho_0\gamma\sin(\theta_0)]\sin(\theta)$$

and finally the linear combination of sine and cosine identity used

$$\begin{aligned} &\rho_0\gamma\cos(\theta-\theta_0)+r\cos(\phi-\theta)=c\cos(\theta+\lambda) \\ &a=r\cos(\phi)+\rho_0\gamma\cos(\theta_0) \\ &b=r\sin(\phi)+\rho_0\gamma\sin(\theta_0) \\ &c=\mathrm{sgn}(a)\sqrt{a^2+b^2} \\ &\lambda=\arctan(-b/a) \end{aligned} \quad .$$

References

Fox, C. (1928). The asymptotic expansion of generalized hypergeometric functions. Proceedings of the London Mathematical Society s2–27 (1):389–400.

Gelfand, A.E., Smith, A.F.M. (1990). Sampling-based approaches to calculating marginal densities. Journal of the American Statistical Association, 85:398–409.

Geman, S., Geman, D. (1984). Stochastic relaxation, Gibbs distributions, and the Bayesian restoration of images. IEEE Transactions on Pattern Analysis and Machine Intelligence, 6(6):721–741.

Gudbjartsson, H., Patz, S., (1995). The Rician distribution of noisy data. Magnetic Resonance in Medicine, 34 (6), 910–914.

Karaman, M.M., Nencka, A.S., Bruce, I.P., Rowe, D.B. (2014). Quantification of the Statistical Effects of Spatiotemporal Processing of Non-task fMRI Data. Brain Connectivity, 4(9):649–661.

Kornak, J., Young, K., Schuff N., Du, A., Maudsley, A.A., Weiner M.W. (2010). K-Bayes reconstruction for perfusion MRI. I: concepts and application. Journal of Digital Imaging, Jun; 23(3):277–86.

Kornak, J. Young, K. (2010). K-Bayes reconstruction for perfusion MRI II: modeling and technical development. Journal of Digital Imaging, Aug; 23(4):374–85.

Kornak, J., Young, K., Soher, B.J., Maudsley, AA (2010). K-space-time reconstruction of MR spectroscopic imaging for enhanced resolution. IEEE Transactions in Medical Imaging, Jul; 29(7):1333–50.

Kornak, J., Young, K., Friedman, E. (2024). Bayesian Image Analysis in Fourier Space. arXiv, stat.ME, 2305.19481.

Lindley, D.V., Smith, A.F.M. (1972). Bayes estimates for the linear model. Journal of the Royal Statistical Society, Series B, 34(1):1–18.

Nencka A.S., Hahn A.D., Rowe D.B. (2009). A Mathematical model for understanding the statistical effects of k-space (AMMUST-k) preprocessing on observed voxel measurements in fcMRI and fMRI. Journal of Neuroscience Methods 181(2):268–282.

O'Hagan A. (1994). Kendall's Advanced Theory of Statistics, vol. 2B. Wiley, New York.

Penny, W.D., Trujillo-Barreto, N.J., Friston, K.J. (2005). Bayesian fMRI time series analysis with spatial priors. Neuroimage, 24(2), 350–362.

Rice, S.O. (1944). Mathematical analysis of random noise. Bell Systems Technological Journal, vol. 23, p. 282.

Rowe, D.B. (2016). Image Reconstruction in Functional MRI. In Handbook of Statistical Methods for Brain Signals and Images, Chapman & Hall/CRC Press, 205–232. ISBN: 978-1-4822-20971

Rowe, D.B., Logan, B.R. (2004). A complex way to compute fMRI activation. Neuroimage 23, 1078–1092.

Rowe, D.B. (2005). Modeling both the magnitude and phase of complex-valued fMRI data. Neuroimage, 25(4), 1310–1324.

Sun J., Kong, M., Pal, S. (2021). The Modified-Half-Normal distribution: Properties and an efficient sampling scheme. Communications in Statistics - Theory and Methods. 52(5):1591–1613.

Von Mises, R. (1918). Uber die Ganzzahligkeit der Atomgewichte und Verwandte Fragen. Physikalische Zeitschrift 19, 490–500.

Yu, C.H., Prado, R., Ombao, H.C., Rowe, D.B. (2023). Bayesian Spatial Modeling via Kernel Convolutions on Complex-Valued fMRI Signals, Biometrics, 79(2):616–628.

Wang, Z., Rowe, D.B., Li X., Brown, D.A. (2024). A Fully Bayesian Approach for Comprehensive Mapping of Magnitude and Phase Brain Activation in Complex-Valued fMRI Data. Magnetic Resonance Imaging, 109:271–285.

Wikipedia (2024a). von Mises distribution. https://en.wikipedia.org/wiki/Von_Mises_distribution. Downloaded May 23, 2024.

Wikipedia (2024b). Modified Half-Normal Distribution. Downloaded May 23, 2024.
https://en.wikipedia.org/wiki/Modified_half-normal_distribution. Downloaded May 23, 2024.

Wikipedia (2024c). List of trigonometric identities.
https://en.wikipedia.org/wiki/List_of_trigonometric_identities. Downloaded May 23, 2024.

Wikipedia (2024d). Inverse-gamma distribution.

https://en.wikipedia.org/wiki/Inverse-gamma_distribution. Downloaded May 23, 2024.
Wright, E.M. (1935). The Asymptotic Expansion of the Generalized Hypergeometric Function. Journal of the London Mathematical Society. s1–10 (4): 286–293.